Title
High-resolution variable-density 3D cones coronary MRA

Journal
Magnetic Resonance in Medicine, 74(3)

ISSN
0740-3194

Authors
Addy, Nii Okai
Ingle, R Reeve
Wu, Holden H
et al.

Publication Date
2015-09-01

DOI
10.1002/mrm.25803

Peer reviewed

HHS Public Access

Author manuscript

Magn Reson Med. Author manuscript; available in PMC 2016 September 01.

Published in final edited form as:

Magn Reson Med. 2015 September ; 74(3): 614–621. doi:10.1002/mrm.25803.

High-Resolution Variable-Density 3D Cones Coronary MRA

Nii Okai Addy[1], **R. Reeve Ingle**[1], **Holden H. Wu**[2], **Bob S. Hu**[1,3], and **Dwight G. Nishimura**[1]

[1]Magnetic Resonance Systems Research Laboratory, Department of Electrical Engineering, Stanford University, Stanford, California

[2]Department of Radiology, University of California, Los Angeles, California

[3]Department of Cardiology, Palo Alto Medical Foundation, Palo Alto, California

Abstract

Purpose—To improve the spatial/temporal resolution of whole-heart coronary MR angiography (CMRA) by developing a variable-density (VD) 3D cones acquisition suitable for image reconstruction with parallel imaging and compressed sensing techniques.

Methods—A VD 3D cones trajectory design incorporates both radial and spiral trajectory undersampling techniques to achieve higher resolution. This design is used to generate a VD cones trajectory with 0.8 mm/66 ms isotropic spatial/temporal resolution, using a similar number of readouts as our previous fully sampled cones trajectory (1.2 mm/100 ms). Scans of volunteers and patients are performed to evaluate the performance of the VD trajectory, using non-Cartesian L_1-ESPIRiT for high-resolution image reconstruction.

Results—With gridding reconstruction, the high-resolution scans experience an expected drop in signal-to-noise and contrast-to-noise ratios, but with L_1-ESPIRiT, the apparent noise is substantially reduced. Compared to 1.2 mm images, in each volunteer, the L_1-ESPIRiT 0.8 mm images exhibit higher vessel sharpness values in the right and left anterior descending arteries.

Conclusion—CMRA with isotropic sub-millimeter spatial resolution and high temporal resolution can be performed with VD 3D cones to improve the depiction of coronary arteries.

Keywords

coronary imaging; 3D cones; trajectory design; parallel imaging

Introduction

Cardiovascular disease is the leading cause of death in the world and is largely contributed to by coronary artery disease (1). Coronary artery disease is typically diagnosed using an invasive X-ray cardiac catheterization procedure. In recent years, there has been an increase in the use of alternative, non-invasive methods for diagnosis, including multi-detector CT angiography (CTA) (2). However, highly attenuating coronary calcification causes a blooming artifact, which is a major factor in reducing the accuracy of CTA (3). Coronary

Address correspondence to: Nii Okai Addy, Packard Electrical Engineering, Room 208, 350 Serra Mall, Stanford, CA 94305-9510, TEL: (650) 725-5638, noaddy@stanford.edu.

MR angiography (CMRA) is not susceptible to such calcium-based artifacts and also provides a non-invasive, radiation-free method for visualizing coronary arteries (4). In its current state, CMRA does not yet provide the same spatial resolution as CT-based methods. Most clinical CMRA protocols image with spatial resolutions in the range of 1.1 – 1.3 mm. (4–7). High resolution is important for coronary angiography in which vessels are typically 2–4 mm in diameter in proximal segments and smaller in distal segments. For CMRA, the challenges of higher resolution imaging include a longer scan time, lower signal-to-noise ratio (SNR), and the requirement for improved motion robustness.

There have been relatively few investigations of sub-millimeter CMRA. Gharib et al. acquired targeted coronary images with a $0.35\times0.35\times1.5$ mm^3 spatial resolution on a 3 T scanner using a Cartesian acquisition with parallel imaging (8). Akçakaya et al. acquired 0.9 mm, isotropic spatial resolution, whole-heart images with a scan time of 6 minutes on a 1.5 T scanner, also using a Cartesian acquisition, but with a compressed sensing reconstruction (9). In addition to parallel imaging and compressed sensing, non-Cartesian imaging provides efficient data acquisition for reduced scan times.

Previously, we developed a CMRA protocol with time-efficient and motion-robust non-Cartesian 3D cones imaging to acquire multi-phasic images of the heart (10). Here we present a method to 1) design a exible, undersampled, variable-density (VD) version of the 3D cones trajectory for time-efficient, high-resolution, sub-millimeter data acquisition and 2) combine parallel imaging and compressed sensing for iterative 3D non-Cartesian image reconstruction using a wavelet-based efficient self-consistent parallel imaging reconstruction (L_1-ESPIRiT) method (11).

Theory

Three key issues to address when increasing the resolution of our 3D cones CMRA acquisition are scan time, SNR, and motion.

Scan Time

Free-breathing, whole-heart CMRA scans are typically acquired with 3DFT or 3D projection reconstruction (3DPR) imaging trajectories. 3DFT is advantageous for the ease with which it can be implemented on the scanner and its ability to encode anisotropic fields of view (FOV). It is not largely affected by off-resonance but is susceptible to ghosting artifacts caused by respiratory motion. Images acquired with the 3DPR trajectory exhibit less coherent motion artifacts than 3DFT. The center of *k*-space is acquired every readout, averaging the effects of motion. However, 3DPR requires undersampling to obtain reasonable CMRA scan times (7,12). The 3D cones trajectory offers the ability to encode anisotropic FOVs with good motion robustness while requiring fewer readouts than 3DFT and 3DPR trajectories (13).

For higher spatial resolution in MR, a larger volume of *k*-space is acquired, increasing the scan time. To maintain the same scan time while increasing the resolution, the data must be undersampled. An efficient VD 3D cones sampling strategy is essential to minimize the resulting aliasing artifacts.

Variable-Density 3D Cones—The 3D cones trajectory consists of 3D spiral trajectories emanating from the center of *k*-space along the surfaces of a set of concentric cones to encode a 3D volume. A single readout of the trajectory is shown in Fig. 1a. The 3D cones trajectory parameters are specified in terms of its transverse (*xy*) and longitudinal (*z*), components. The main parameters of 3D cones design are the FOVs (FOV_{xy} and FOV_z), and spatial resolutions (res_{xy} and res_z).

For whole-heart imaging in an axial slab, the elevation angles of the concentric conic surfaces are chosen to encode an anisotropic, near-rectangular FOV (14). For the variable-density design, the set of angles is undersampled by reducing the prescribed FOV (15)

For each conic surface, a spiral trajectory is designed using a gradient twist function, G_{twist}, which indicates the degree of rotation in the transverse plane as the *k*-space radius increases as shown in Fig. 1a (13, 16). For a standard, fully sampled trajectory, the original equation describing the gradient twist function for the cone surface *n* can be written as:

$$G_{twist,n}(\boldsymbol{k})=\frac{G_{circ,n}(\boldsymbol{k})}{G_{rad,n}(\boldsymbol{k})}=\sqrt{\max\left[\left(\frac{2\pi\sin(\theta_n)|\boldsymbol{k}|\mathrm{FOV}_{rad,n}}{L_n}\right)^2-1,0\right]} \quad (1)$$

G_{circ} and G_{rad} are the circumferential and radial components of the trajectory gradient, *L* is the number of interleaves projected onto a conic surface with elevation angle θ, *k* is the *k*-space location, and FOV_{rad} is the radial FOV based on the desired shape of the anisotropic FOV.

In the proposed VD 3D cones design, similar to previous VD 2D spiral design (17), the FOV (sampling density) encoding varies as a function of $|\boldsymbol{k}|$. $FOV_{rad,n}$ in Eq. 1 is replaced with ρ_{rad}, which represents the variable sampling density.

$$G_{twist,n}(\boldsymbol{k})=\sqrt{\max\left[\left(\frac{2\pi\sin(\theta_n)|\boldsymbol{k}|\rho_{rad,n}(\boldsymbol{k})}{L_n}\right)^2-1,0\right]} \quad (2)$$

Sampling up to a larger k_{max} increases the spatial resolution, which is the goal of the VD design in this application. When keeping all the other parameters constant, this increases the readout duration. Because G_{twist} is the ratio of circumferential to radial components of the trajectory gradients, for lower G_{twist} values, fewer points are required to reach k_{max}. G_{twist} is proportional to ρ_{rad}, so by reducing ρ_{rad}, high-resolution data can be acquired without increasing the scan time. Undersampling occurs when the sampling density $\rho_{rad} < FOV_{rad}$, but strategically reducing ρ as a function of *k* can result in only subtle aliasing artifacts. An example of a projected spiral designed for uniform and variable sampling densities is shown in Fig. 1a.

SNR—The SNR of an imaging protocol is proportional to the voxel volume; thus, for a 3D acquisition, an isotropic reduction in the voxel dimensions rapidly decreases the SNR. Additionally, noise-like aliasing artifacts arise from undersampling the 3D cones trajectory.

Nonlinear reconstruction with parallel imaging and compressed sensing can help suppress aliasing artifacts and increase the apparent SNR of the reconstructed images.

Motion—In addition to respiratory-based motion, contractile motion is another factor affecting the image quality of CMRA. CMRA sequences are triggered to acquire data typically during an 80 to 150 ms window in the cardiac cycle when the heart is relatively still, yet some motion does occur. Increasing the temporal resolution can help preserve the desired spatial resolution by limiting the extent of contractile motion-induced blurring. This leads to longer total scan times, as fewer readouts are acquired each heartbeat. The time-efficiency of the VD 3D cones design can help counteract the time penalty incurred from increasing the temporal resolution.

Methods

VD 3D Cones Trajectory Design

Our previous implementation of 3D cones CMRA used a fully sampled trajectory encoding a $28 \times 28 \times 14$ cm^3 FOV with 1.2 mm isotropic resolution. Data were acquired with 9,142 readouts using a 2.8 ms trajectory waveform duration (10). The target resolution for the proposed method was 0.8 mm isotropic. For this resolution, a fully sampled 3D cones trajectory required 27,483 readouts.

For the proposed VD trajectory, full sampling was prescribed up to k_1=90 m^{-1} (14% of k_{max}) to provide the calibration data for L_1-ESPIRiT. The sampling density function shown in Fig. 1b was parameterized as a 10th order polynomial with a sampling density of 0.59 at k_{max} also used as the undersampling factor for the number of conic surfaces. The parameters were manually adjusted to generate a trajectory with a similar number of readouts as our previous implementation. The resulting VD trajectory, comprised of 9,591 readouts, had a corresponding acceleration factor of 2.9 compared to a fully sampled trajectory. Imaging with 3DFT and 3DPR trajectories using the same FOV, spatial resolution, and the number of readout parameters would require acceleration factors of 6.4 and 12.2, respectively.

Iterative Reconstruction

Previously, CG-SENSE (18) and SPIRiT (19) reconstructions have been applied to arbitrary *k*-space trajectory acquisitions. ESPIRiT, a recently developed method, can also easily be combined with a sparsity constraint. Referred to as L_1-ESPIRiT, this method provides efficient parallel imaging reconstruction with compressed sensing (11). Previously, successful results have been achieved with compressed sensing for non-Cartesian center-out trajectories such as 2D spirals and 3DPR (20, 21).

The first step of L_1-ESPIRiT is the computation of coil sensitivity maps based on a fully sampled calibration region at the *k*-space origin. For the 3D cones trajectory, acquired data is gridded in *k*-space and cropped to the calibration region then input to the coil sensitivity calculation algorithm. Following coil sensitivity calculation, images are reconstructed iteratively by setting up the data acquisition process as the inverse problem:

$$\arg\min_{m}\sum_{i=1}^{N}\|y_i - AS_i m\|_2^2 + \lambda\|\Psi m\| \quad (3)$$

With a set of N coil sensitivity maps S, an image m is reconstructed using a regularized CG-SENSE-like algorithm (18). y is the multi-channel, acquired data, and A is the inverse gridding operation. A wavelet transform Ψ is used for the sparsity constraint and is weighted by a constant λ. Figure 2 outlines the reconstruction procedure adapted for VD 3D cones CMRA.

The calibration data were run through the Software Toolbox and Programming Library for Compressed Sensing and Parallel Imaging to generate a single set of coil sensitivity maps (22). A wavelet-based reconstruction method based on the fast iterative soft-thresholding algorithm (FISTA) (23) was implemented to perform L_1-regularized iterative reconstruction (20). At each step, soft-thresholding was applied to randomly shifted Cohen-Daubechies-Feauveau (CDF) 9/7 wavelets of the current image estimate (24, 25). The computational demand for the high-resolution 3D images prevented subband-dependent thresholding. Modifications to the freely available MATLAB (MathWorks, Natick, MA) code were made to support 3D processing [http://bigwww.epfl.ch/algorithms/mri-reconstruction/]. Conditioning in the form of density compensation for the non-Cartesian acquisition was included in the processing to increase the convergence rate of the reconstruction algorithm. Uniformly calculated sample density weights were calculated using a GPU implementation of the convolution method over four iterations using a four-lobe kernel (26,27). Post-processing ran on a Linux system with dual 2.6 GHz Xeon x5650 CPUs and 72 GB RAM. Coil sensitivity estimation took 4 min, and the fast wavelet-based reconstruction method took approximately 30 min for one cardiac phase.

In-Vivo Studies

Scans were run on 1.5 T (GE Signa Excite and Signa Twinspeed) scanners with an 8-channel cardiac array coil using an alternating TR-SSFP sequence (10). Scan parameters were set to $TE/TR_1/TR_2$ = 0.57/1.15/4.33 ms, 70° flip angle, and 2.8 ms readout waveform durations. Three cardiac phases with 12 readouts per phase per cardiac cycle were acquired with a temporal resolution of 66 ms, a 1.5-fold improvement over our previous temporal resolution of 100 ms. 2D iNAVs were acquired each heartbeat for respiratory-based motion tracking. A sagittal iNAV was acquired preceding the 3D cones acquisition and a coronal iNAV was acquired following the 3D cones acquisition. A 3D translation motion trajectory was extracted from the series of 2D iNAVs using a multiple reference iNAV method (28). Retrospective motion correction was executed using linear phase modulation (10). To account for eddy current-based trajectory errors, the gradient systems were characterized with linear time-invariant models to estimate the trajectories produced by the scanners (29).

To assess the improvement in spatial resolution for high-resolution VD 3D cones imaging, three volunteers were scanned both at a 1.2 mm isotropic resolution with a standard 3D cones trajectory and a 0.8 mm isotropic resolution with the proposed VD 3D cones trajectory. For each volunteer, both datasets were acquired in the same exam. In addition to

the volunteer subjects, four patients suspected of coronary artery disease were scanned with the high-resolution trajectory only. Subjects gave written consent approved by the Institutional Review Board. The patient ages ranged from 50 to 67 with one patient being female. The high-resolution CMRA scan was added to the patients' standard clinical exam protocols, which included the administration of gadobenate dimeglumine. The CMRA sequence was run following the injection of the contrast agent to take advantage of the increased blood signal. Depending on the exam, the post-contrast CMRA scan commenced 1 to 15 minutes following contrast injection.

Phantom Study

To provide a reference to the in-vivo studies, a resolution phantom containing vials with varying diameters was imaged with the 1.2 mm fully sampled and 0.8 mm VD 3D cones trajectories (30). The phantom contained five groups of five vials of nickel-chloride-doped water. The diameters in each group were 0.75, 1.5, 2.25, 4, and 6 mm. Phantom images were acquired in two modes. First, data was acquired continuously without ECG triggering. Second, data was ECG triggered to a simulated heart rate of 80 beats per minute while the scanner table was programmed to move cyclically over a maximum distance of 20 mm with a period of 4.5 sec. 2D iNAVs were acquired in the same manner as the in-vivo case for retrospective motion correction that was tracked from additional cylindrical, rectangular, and GE resolution phantoms imaged along with the vials. For the phantom study, 1.2 mm images were reconstructed with gridding and 0.8 mm images were reconstructed with L_1-ESPIRiT.

In addition to the scanner images, images were simulated at the two resolutions based on the analytic forms of the Fourier transform of a cylinder (31). The simulated images were based solely on the spatial resolutions and not on the corresponding 3D cones trajectories.

Vessel Sharpness

For CMRA, the image sharpness of coronary arteries is often calculated as the inverse of the average transition width of the coronary lumen profile (32, 33). The transition width is defined as the distance along a profile from 20% to 80% of the peak to minimum signal of the lumen. For this metric, higher values indicate sharper edges.

Vessel sharpness values were calculated for 1.2 mm resolution images reconstructed with gridding and 0.8 mm resolution images reconstructed with L_1-ESPIRiT using the CoroEval software (34). Before processing with CoroEval, images were interpolated to an isotropic resolution of 0.4 mm. In-vivo measurements were made in the right coronary arteries (RCA) and left anterior descending arteries (LAD). Measurements were also made in the phantom and simulated images.

Signal and Contrast

The SNR and blood to myocardium contrast-to-noise ratios (CNR) were measured for 1.2 mm and 0.8 mm in-vivo images reconstructed with gridding only. Measurements of the signal intensity were made in regions of interest (ROI) in the left ventricle (LV), right ventricle (RV), myocardium, and background.

Results

In comparing the 1.2 and 0.8 mm volunteer acquisitions reconstructed with gridding, there is a significant decrease in SNR at the higher resolution, as demonstrated in Fig. 3. The SNR loss is from the 74% decrease in voxel volume and trajectory undersampling, which produces noise-like aliasing artifacts. Figure 4 shows the measured SNR and CNR in the LV and RV of the subject studies. In the volunteers that were imaged at both spatial resolutions, the ratio of the SNR in the 0.8 mm gridded images to that in the 1.2 mm gridded images is 0.35±0.01 in the LV and 0.32±0.02 in the RV. The ratio of CNRs is 0.22±0.03 in the LV and 0.26±0.04 in the RV. The ratios of SNR are slightly higher than the theoretical prediction of 0.26. After iterative reconstruction, the image noise is less apparent, but with nonlinear processing, the SNR of L_1-ESPIRiT images cannot be directly compared to images reconstructed with gridding.

The scan times of the in-vivo, high-resolution scans were 13.4±2 min, similar to 12.9±4.3 min scan times in the 131 patient CMRA trial by Sakuma et al. (4). The high-resolution datasets were reconstructed with gridding and L_1-ESPIRiT. Figure 5 shows the resulting images from four subjects. For each subject, the images are displayed with an identical window level.

Figure 6 shows the in-vivo vessel sharpness measurements for all the subjects. The values vary by subject and by coronary artery. For each volunteer imaged with both resolutions, the average vessel sharpness value is higher in the L_1-ESPIRiT 0.8 mm image than in the 1.2 mm image. The factor increase is 1.22±0.01 in the RCA and 1.16±0.01 in the LAD. To visually demonstrate the vessel sharpness improvement at the higher resolution, in the bottom row of Fig. 3, a branch of the RCA in volunteer A can be observed more clearly with 0.8 mm resolution than with 1.2 mm resolution.

The results of the phantom experiment are shown in Fig. 7. Aside from the presence of air bubbles and banding artifacts mainly in the larger vials, the phantom images in Fig. 7b closely resemble the simulated images in Fig. 7a including the effects of Gibb's ringing. Both the absolute vessel sharpness and improvement in vessel sharpness from increasing the spatial resolution vary in the phantom by vial diameter as shown in 7c. The 0.75 mm diameter vials exhibit the highest vessel sharpness, while the 4 and 6 mm diameter vials exhibit the largest improvement from increased resolution. Acquiring the phantoms in the presence of motion reduces the measured vessel sharpness. The blurring effect is larger for the 0.8 mm resolution acquisitions, which show an average loss in vessel sharpness of 16% compared to 5% in the 1.2 mm images. The average improvement in vessel sharpness with increased spatial resolution is 1.37±0.10 in simulation, 1.28±0.07 in the stationary phantom, and 1.13±0.06 in the phantom with motion.

Discussion

A high-resolution CMRA method has been presented using a variable-density 3D cones acquisition in combination with L_1-ESPIRiT to obtain images with 0.8 mm isotropic resolution. The acceleration factor of 2.9 for a 0.8 mm VD 3D cones trajectory is lower than

acceleration factors of 6.4 for 3DFT and 12.2 for 3DPR required to image in the same scan time.

The initial high-resolution images reconstructed with gridding do not exhibit large coherent aliasing artifacts. Rather, the presence of artifacts is noise-like. Figure 3 shows both the increased image noise and the improved vessel clarity from the previously implemented 1.2 mm resolution to the proposed 0.8 mm resolution. Compared to gridding, with L_1-ESPIRiT, the appearance of noise is reduced. For context, the RCA diameter at the slice shown in the Fig. 3 is 3 mm as measured with the CoroEval software. Compared to the lower resolution image, the signal intensity across the lumen of the RCA is more uniform in the high-resolution image. This agrees with the vessel sharpness value which in this case was a factor of 1.24 larger for the 0.8 mm resolution image.

In this study, vessel sharpness is measured based on the transition width of the lumen signal intensity profile. Although, this provides a measure of the achieved resolution, the goal of the proposed method is to better assess the degree of stenosis. However, no stenoses were found in the relatively small sample size of patients imaged in this preliminary study.

As the phantom study shows, the main factor affecting image quality improvement with the proposed method is the occurrence of motion. With motion present, the measured vessel sharpness decreases in every case with a larger penalty at the 0.8 mm resolution. Possible causes may include insufficient motion estimate precision from the 3.2 mm resolution 2D iNAVs interpolated to 1.6 mm or temporal interpolation error between 2D iNAVs preceding and following the acquisition window. One possible option is to apply the trajectory design and iterative reconstruction methods from the proposed VD 3D cones framework for 2D spiral imaging to improve the resolution of the 2D iNAVs and the precision of the motion estimates. In-vivo, the retrospective motion correction uses 3D translational motion and does not directly correct nonrigid motion of the heart. An autofocus correction method has been proposed that has the ability to optimize correction in different regions of the heart, but has a high computational demand and cannot easily be combined with iterative reconstruction (30).

The richness of the 3D cones trajectory permits a wide range of VD designs, not yet demonstrated in this work. The transverse and longitudinal components of the trajectory can be individually parameterized, thus the sampling density could be a function of both k_{xy} and k_z. Also, it is possible to trade-off the sampling density of the projected spirals with the degree of undersampling of the conic surfaces, which could have implications for the resulting aliasing patterns.

The multi-phasic acquisition performed in our CMRA protocol provides additional information that could be taken advantage of in the reconstruction process. Currently, images are reconstructed individually by cardiac phase. Strategies combining data from the various phases could be beneficial in improving the image quality of the iterative reconstruction process (35).

Conclusion

Using a novel VD 3D cones trajectory accelerated by a factor of 2.9 compared to a fully sampled trajectory, the isotropic spatial resolution of our CMRA scan run on a 1.5 T scanner with 8 receiver channels was increased from 1.2 to 0.8 mm and the temporal resolution was increased from 100 to 66 ms. Using L_1-ESPIRiT, images were reconstructed displaying sharper vessels than at the previous spatial and temporal resolutions despite the reduction in SNR. Future work includes integration with advanced motion correction techniques and validation of the method in the clinical setting.

Acknowledgments

We would like to thank Joseph Cheng and Tao Zhang for helpful discussion on implementing L_1-ESPIRiT and the referees for providing insightful and pertinent comments. This work was supported by NIH T32 HL007846 and GE Healthcare.

References

1. Mendis, S.; Puska, P.; Norrving, B., editors. Global atlas on cardiovascular disease prevention and control. World Health Organization; Geneva: 2011.
2. Rochitte CE, George RT, Chen MY, Arbab-Zadeh A, Dewey M, Miller JM, Niinuma H, Yoshioka K, Kitagawa K, Nakamori S, Laham R, Vavere AL, Cerci RJ, Mehra VC, Nomura C, Kofoed KF, Jinzaki M, Kuribayashi S, de Roos A, Laule M, Tan SY, Hoe J, Paul N, Rybicki FJ, Brinker JA, Arai AE, Cox C, Clouse ME, Di Carli MF, Lima JAC. Computed tomography angiography and perfusion to assess coronary artery stenosis causing perfusion defects by single photon emission computed tomography: the CORE320 study. European Heart Journal. 2014; 35:1120–1130. [PubMed: 24255127]
3. Hoffmann U, Ferencik M, Cury RC, Pena AJ. Coronary CT angiography. Journal of Nuclear Medicine. 2006; 47:797–806. [PubMed: 16644750]
4. Sakuma H, Ichikawa Y, Chino S, Hirano T, Makino K, Takeda K. Detection of coronary artery stenosis with whole-heart coronary magnetic resonance angiography. J Am Coll Cardiol. 2006; 48:1946–1950. [PubMed: 17112982]
5. Yang Q, Li K, Liu X, Bi X, Liu Z, An J, Zhang A, Jerecic R, Li D. Contrast-enhanced whole-heart coronary magnetic resonance angiography at 3. 0-T: a comparative study with X-ray angiography in a single center. J Am Coll Cardiol. 2009; 54:69–76. [PubMed: 19555843]
6. Kato S, Kitagawa K, Ishida N, Ishida M, Nagata M, Ichikawa Y, Katahira K, Matsumoto Y, Seo K, Ochiai R, Kobayashi Y, Sakuma H. Assessment of coronary artery disease using magnetic resonance coronary angiography: a national multicenter trial. J Am Coll Cardiol. 2010; 56:983–991. [PubMed: 20828652]
7. Piccini D, Monney P, Sierro C, Coppo S, Bonanno G, van Heeswijk RB, Chaptinel J, Vincenti G, de Blois J, Koestner SC, Rutz T, Littmann A, Zenge MO, Schwitter J, Stuber M. Respiratory self-navigated postcontrast whole-heart coronary MR angiography: initial experience in patients. Radiology. 2014; 270:378–386. [PubMed: 24471387]
8. Gharib AM, Abd-Elmoniem KZ, Ho VB, Födi E, Herzka DA, Ohayon J, Stuber M, Pettigrew RI. The feasibility of 350 μm spatial resolution coronary magnetic resonance angiography at 3 T in humans. Invest Radiol. 2012; 47:339–345. [PubMed: 22551651]
9. Akçakaya M, Basha TA, Chan RH, Manning WJ, Nezafat R. Accelerated isotropic sub-millimeter whole-heart coronary MRI: Compressed sensing versus parallel imaging. Magnetic Resonance in Medicine. 2014; 71:815–822. [PubMed: 23440946]
10. Wu HH, Gurney PT, Hu BS, Nishimura DG, McConnell MV. Free-breathing multiphase whole-heart coronary MR angiography using image-based navigators and three-dimensional cones imaging. Magn Reson Med. 2013; 69:1083–1093. [PubMed: 22648856]

11. Uecker M, Lai P, Murphy MJ, Virtue P, Elad M, Pauly JM, Vasanawala SS, Lustig M. ESPIRiT-an eigenvalue approach to autocalibrating parallel MRI: Where SENSE meets GRAPPA. Magnetic Resonance in Medicine. 2014; 71:990–1001. [PubMed: 23649942]
12. Pang J, Bhat H, Sharif B, Fan Z, Thomson LEJ, LaBounty T, Friedman JD, Min J, Berman DS, Li D. Whole-heart coronary MRA with 100% respiratory gating efficiency: Self-navigated three-dimensional retrospective image-based motion correction (TRIM). Magnetic Resonance in Medicine. 2014; 71:67–74. [PubMed: 23401157]
13. Gurney PT, Hargreaves BA, Nishimura DG. Design and analysis of a practical 3D cones trajectory. Magn Reson Med. 2006; 55:575–582. [PubMed: 16450366]
14. Larson PZ, Gurney PT, Nishimura DG. Anisotropic field-of-views in radial imaging. IEEE Trans Med Imaging. 2008; 27:47–57. [PubMed: 18270061]
15. Scheffler K, Hennig J. Reduced circular field-of-view imaging. Magn Reson Med. 1998; 40:474–480. [PubMed: 9727952]
16. Gurney, PT. PhD thesis. Stanford University; United States – California: 2007. Magnetic resonance imaging using a 3D cones *k*-space trajectory.
17. Spielman DM, Pauly JM, Meyer CH. Magnetic resonance uoroscopy using spirals with variable sampling densities. Magn Reson Med. 1995; 34:388–394. [PubMed: 7500878]
18. Prüssmann KP, Weiger M, Börnert P, Boesiger P. Advances in sensitivity encoding with arbitrary k-space trajectories. Magn Reson Med. 2001; 46:638–651. [PubMed: 11590639]
19. Lustig M, Pauly JM. SPIRiT: Iterative self-consistent parallel imaging reconstruction from arbitrary k-space. Magn Reson Med. 2010; 64:457–471. [PubMed: 20665790]
20. Guerquin-Kern M, Haberlin M, Prüssmann KP, Unser M. A fast wavelet-based re-construction method for magnetic resonance imaging. IEEE Transactions on Medical Imaging. 2011; 30:1649–1660. [PubMed: 21478074]
21. Nam S, Akçakaya M, Basha T, Stehning C, Manning WJ, Tarokh V, Nezafat R. Compressed sensing reconstruction for whole-heart imaging with 3D radial trajectories: a graphics processing unit implementation. Magn Reson Med. 2013; 69:91–102. [PubMed: 22392604]
22. Uecker, M.; Virtue, P.; Ong, F.; Murphy, MJ.; Alley, MT.; Vasanawala, SS.; Lustig, M. Software toolbox and programming library for compressed sensing and parallel imaging. ISMRM Workshop on Data Sampling and Image Reconstruction; Sedona, Arizona. 2013;
23. Beck A, Teboulle M. A fast iterative shrinkage-thresholding algorithm for linear inverse problems. SIAM Journal on Imaging Sciences. 2009; 2:183–202.
24. Cohen A, Daubechies I, Feauveau JC. Biorthogonal bases of compactly supported wavelets. Communications on pure and applied mathematics. 1992; 45:485–560.
25. Chambolle A, DeVore R, Lee NY, Lucier B. Nonlinear wavelet image processing: variational problems, compression, and noise removal through wavelet shrinkage. Image Processing, IEEE Transactions on. 1998; 7:319–335.
26. Pipe JG, Menon P. Sampling density compensation in MRI: rationale and an iterative numerical solution. Magn Reson Med. 1999; 41:179–186. [PubMed: 10025627]
27. Johnson KO, Pipe JG. Convolution kernel design and efficient algorithm for sampling density correction. Magn Reson Med. 2009; 61:439–447. [PubMed: 19165893]
28. Ingle, RR.; Addy, NO.; Wu, HH.; Hu, BS.; Nishimura, DG. Optimized navigator motion estimation for coronary MRA. Proceedings of the 25th International MR Angiography Workshop; New York, New York. 2013; p. 88
29. Addy NO, Wu HH, Nishimura DG. Simple method for MR gradient system characterization and *k*-space trajectory estimation. Magnetic Resonance in Medicine. 2012; 68:120–129. [PubMed: 22189904]
30. Ingle RR, Wu HH, Addy NO, Cheng JY, Yang PC, Hu BS, Nishimura DG. Nonrigid autofocus motion correction for coronary MR angiography with a 3D cones trajectory. Magn Reson Med. 2014; 72:347–361. [PubMed: 24006292]
31. Koay CG, Sarlls JE, Ozarslan E. Three-dimensional analytical magnetic resonance imaging phantom in the fourier domain. Magn Reson Med. 2007; 58:430–436. [PubMed: 17616967]
32. Rodenwaldt J, Kopka L, Meyer HJ, Vosshenrich R, Funke M, Grabbe E. Determination of contour clarity in contrast-enhanced MR angiography: definition and clinical evaluation exemplified by

ECG-triggered imaging of the thoracic aorta. RöFo : Fortschritte auf dem Gebiete der Röntgenstrahlen und der Nuklearmedizin. 1998; 169:616–21. [PubMed: 9930215]

33. Deshpande VS, Wielopolski PA, Shea SM, Carr J, Zheng J, Li D. Coronary artery imaging using contrast-enhanced 3D segmented EPI. Journal of Magnetic Resonance Imaging. 2001; 13:676–681. [PubMed: 11329188]
34. Schwemmer C, Forman C, Wetzl J, Maier A, Hornegger J. CoroEval: a multi-platform, multi-modality tool for the evaluation of 3D coronary vessel reconstructions. Physics in Medicine and Biology. 2014; 59:5163. [PubMed: 25138652]
35. Yeung, S.; Addy, NO.; Ingle, RR.; Hu, BS.; Nishimura, DG. Nonrigid 3D+t image registration for temporal averaging in multiphase coronary MR angiography. Proceedings 22nd Scientific Meeting, International Society for Magnetic Resonance in Medicine; Milan, Italy. May 2014; p. 2389

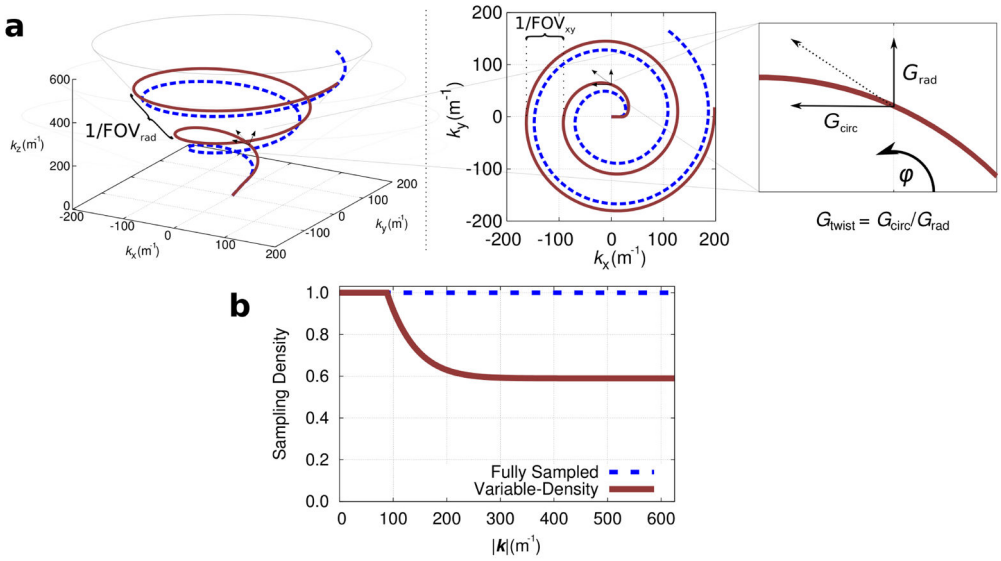

Figure 1.

The path of the 3D cones trajectory on each conic surface is determined based on G_{twist}, which is the ratio of circumferential to radial movement (a). A variable-density trajectory is generated by reducing G_{twist}, which increases the spacing between loops of the projected spiral. A single readout path from fully sampled and variable-density trajectories is displayed. The sampling density functions for the two trajectories are also displayed (b).

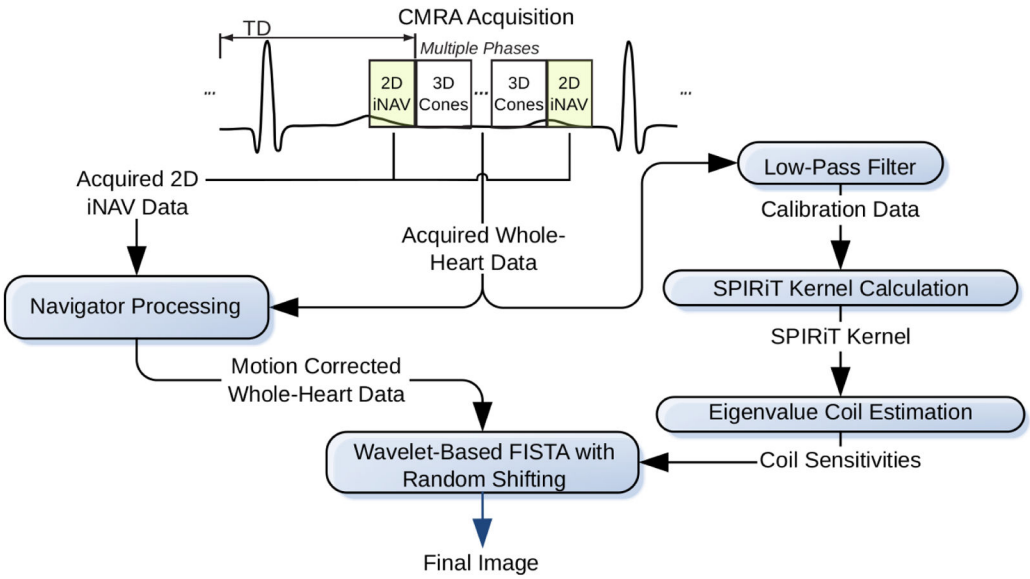

Figure 2.

L_1-ESPIRiT adapted for VD 3D cones CMRA. The left of the diagram illustrates the 2D image-based motion correction. The right of the diagram illustrates the calculation of coil sensitivity maps. Iterative reconstruction is performed using a method based on FISTA in the final step.

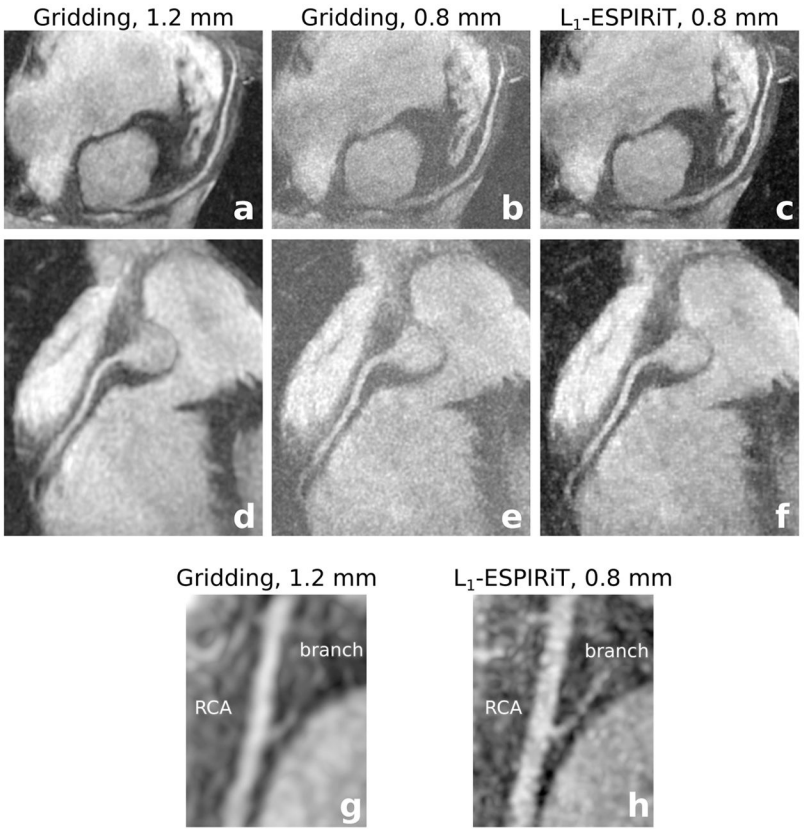

Figure 3.

A comparison of reformatted, maximum intensity projection (MIP), volunteer images of the LAD (a–c) and RCA (d–h) acquired with 1.2 and 0.8 mm isotropic resolutions. The 1.2 mm resolution images were reconstructed with gridding and the 0.8 mm resolution images were reconstructed with both gridding and L_1-ESPIRiT. An additional reformat (g,h) is displayed at both resolutions showing a branch of the RCA.

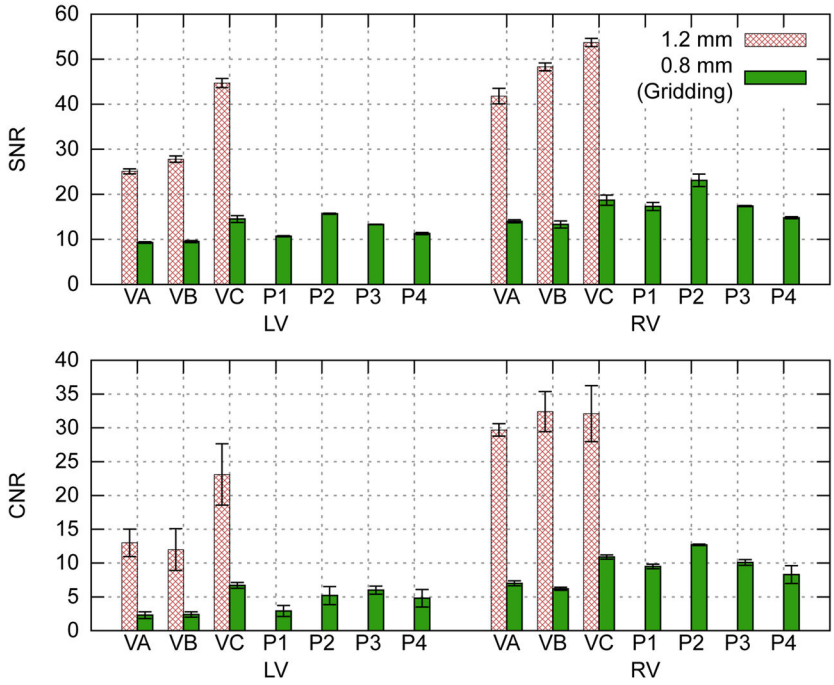

Figure 4.

SNR and blood-to-myocardium CNR measurements in the left ventricle (LV) and right ventricle (RV) in gridded images with 1.2 and 0.8 mm resolution. Measurements from all three cardiac phases are included. The error bars indicate the standard error of the mean.

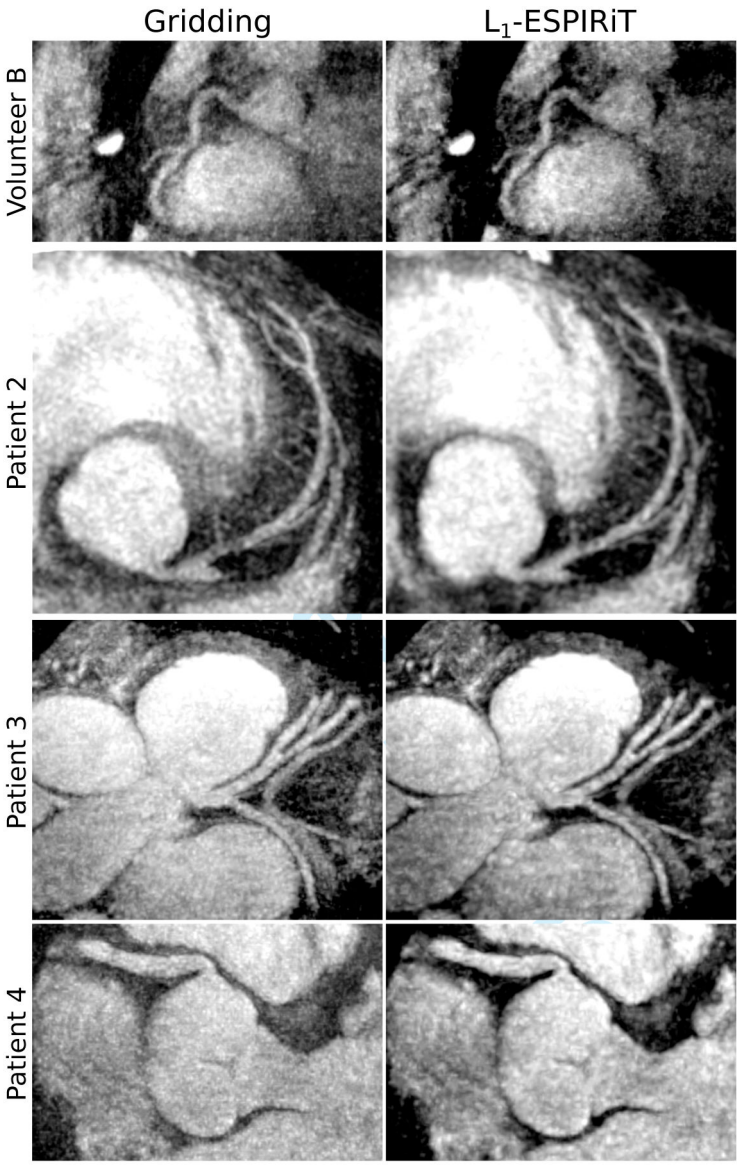

Figure 5.
Reformatted, 0.8 mm resolution, MIP images reconstructed with gridding (left) and L_1-ESPIRiT (right).

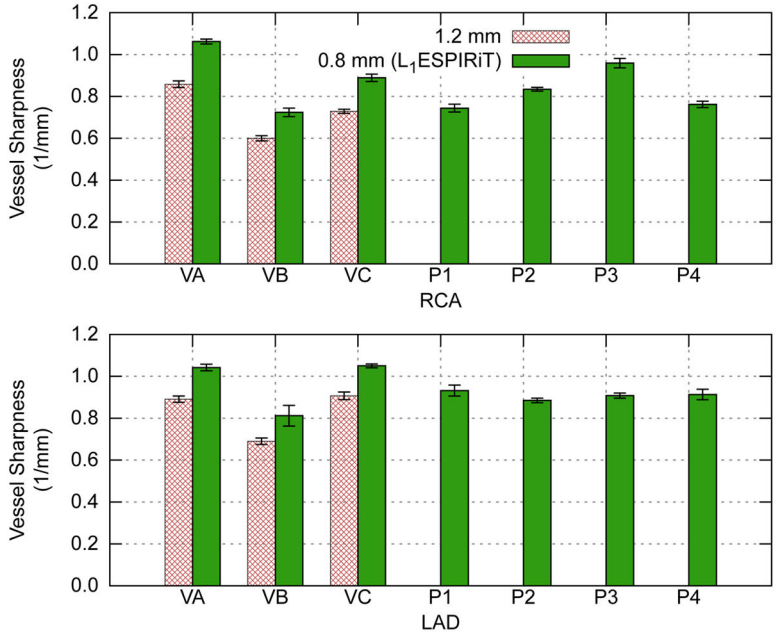

Figure 6.

Right coronary (RCA) and left anterior descending (LAD) artery vessel sharpness measured in volunteers (V) and patients (P). Measurements are based on a single cardiac phase of 1.2 mm resolution images reconstructed with gridding and 0.8 mm resolution images reconstructed with L_1-ESPIRiT. Patients were scanned with the high-resolution trajectory only. The CoroEval software evaluates the vessel sharpness along an artery in 1 mm segments. The error bars on the plot indicate the standard error of the mean. Higher values correspond to a sharper vessel depiction.

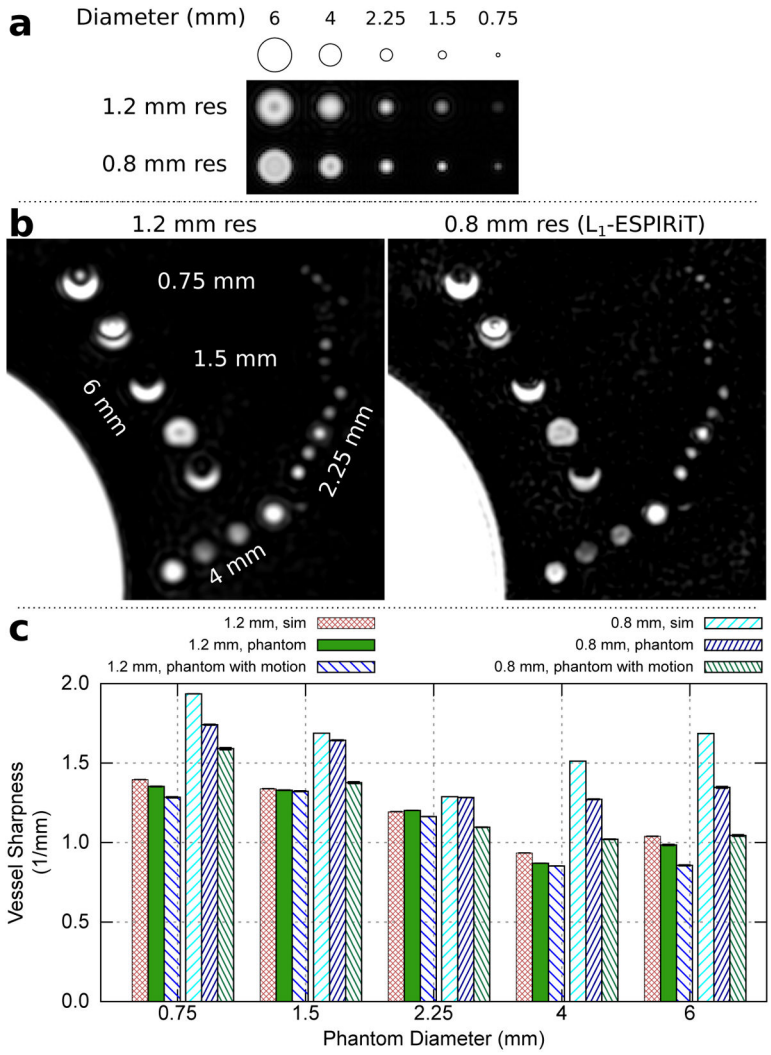

Figure 7.

0.75, 1.5, 2.25, 4, and 6 mm diameter cylindrical phantoms simulated (a) and imaged (b) with 1.2 and 0.8 mm resolutions. Phantom images are displayed for the stationary case. Air bubbles and banding artifacts are present in the larger vials, and low signal regions within these vials are a result of Gibbs phenomenon. Vessel sharpness measurements are shown for simulated images and phantom images with and without motion present at both resolutions (c). The error bars indicate the standard error of the mean.